Phonon dispersion, Raman spectra, and evidence for spin-phonon coupling in MnV_2O_4 from first principles

Dibyendu Dey [1,2,*] T. Maitra,[3] U. V. Waghmare,[4] and A. Taraphder[1,5,6]

[1]*Department of Physics, Indian Institute of Technology Kharagpur, Kharagpur 721302, India*

[2]*Department of Physics, Arizona State University, Tempe, Arizona 85287, USA*

[3]*Department of Physics, Indian Institute of Technology Roorkee, Roorkee 247667, India*

[4]*Theoretical Sciences Unit, Jawaharlal Nehru Centre for Advanced Scientific Research, P.O. Jakkur, Bangalore 560064, India*

[5]*Centre for Theoretical Studies, Indian Institute of Technology Kharagpur, Kharagpur 721302, India*

[6]*School of Basic Sciences, Indian Institute of Technology Mandi, Himachal Pradesh 175001, India*

(Received 2 May 2019; revised manuscript received 28 January 2020; accepted 6 May 2020; published 19 May 2020)

MnV_2O_4 in the spinel structure is known to exhibit coupled orbital and spin ordering and its Raman spectra show interesting anomalies in its low-temperature phase. With a goal to explain this behavior involving coupled spins and phonons, we determine here the spin-phonon couplings in MnV_2O_4 from a theoretical analysis of its phonon spectra and their dependence on spin ordering and electron correlations, obtained from first-principles density functional theoretical calculations. Using these in an analysis based on a Landau-like theory, we uncover the mechanism governing the Raman anomalies observed in its low-temperature phase.

DOI: 10.1103/PhysRevB.101.205132

I. INTRODUCTION

Correlated electronic systems with spinel structure have seen a surge in interest of late, due to inherently rich physics involving frustrated magnetism, orbital ordering, charge ordering, etc. Fascinating physical phenomena emerge from the coupling between various degrees of freedom such as spin, orbital, and lattice, in the presence of both geometric frustration and Coulomb correlation [1–6]. The competition among different degrees of freedom manifests itself in several structural and magnetic transitions accompanied by orbital ordering in these systems [7–10]. These compounds, having the generic formula AB_2O_4, consist of two distinct cation sites: the A site is tetrahedrally coordinated with neighboring O sites while B site is octahedrally coordinated with O ligands [11], as shown schematically in Fig. 1(a). Geometrically frustrated magnetic spinels provide a fertile playground for exploration of interplay between these degrees of freedom [12,13].

MnV_2O_4 is a member of the AB_2O_4 family, which has the A site (Mn^{+2}, $S = 5/2$) magnetic but not orbitally active, while the B site (V^{+3}, $S = 1$) is both magnetic and orbitally active. The combined effect of magnetic and orbital degrees brings in rich and complex physics. This compound undergoes a magnetic transition from the paramagnetic (PM) to collinear ferrimagnetic (FiM) phase at $T_{N1} = 57$ K, followed by a structural transition (cubic $\rightarrow$ tetragonal) together with a second magnetic transition at $T_{N2} = 54$ K, where noncollinear FiM spin ordering sets in [10,14,15].

Earlier, the controversies mostly centered around the ordering of orbitals of V and stimulated an upsurge of research in this system [10,15,16]. Various possible scenarios were proposed for the orbital order based on the symmetry of the tetragonal phase and the type of dominant interactions [10,15]. In a recent theoretical study [17], A-type antiferro-orbital ordering has been observed at the V sites where one t_{2g} electron occupies the d_{xy} orbital at every V site and other electron occupies d_{xz} and d_{yz} orbitals alternately along the c direction. These findings are in good agreement with the experimental measurements in MnV_2O_4 [10].

Though much attention has been given to the electronic properties, the phonon-related phenomena and their coupling with other degrees of freedom remained unexplored. However, a few fascinating experiments performed in the recent past indicate that phonons play an important role at the microscopic level. Takubo *et al.* [18] investigated Raman scattering of MnV_2O_4 and observed that several peaks evolve in the Raman spectra below T_{N2}. They showed a peculiar polarization dependence of B_g modes and tried to explain it with Mott excitation phenomena. However, the appearance of an experimental intensity peak with XY polarization was not supported by their analysis. Their mode assignment of the Raman-active peaks in the tetragonal phase was based on the $I4_1/amd$ space group, whereas the space group symmetry of MnV_2O_4 is $I4_1/a$ [10]. Later, an inelastic light scattering study of the temperature and magnetic field dependencies of one- and two-magnon excitations in MnV_2O_4 revealed that spin-lattice coupling is indeed significant in its low-temperature phase [19]. Additionally, anomalous temperature dependence of the peak intensity was observed which was attributed to a strong coupling between magnetic and vibrational excitations in MnV_2O_4.

In view of the significant effects of phonons in this system, we have investigated the spin-phonon coupling across the

*ddey3@asu.edu

Brillouin zone (BZ), along with Raman scattering to understand the polarization dependence of B_g modes from density functional theory (DFT) calculations. The paper is organized as follows. In Sec. II, we briefly discuss the methodology used to calculate phonons and related properties. In Sec. III, first, we discuss the structural properties in detail and calculate phonon modes at the Γ point of the BZ. Next we present an analysis of Raman scattering intensities of the B_g mode. Later, we study the effects of spin-phonon coupling and calculate the coupling term at different high-symmetry points of the BZ and compare our results with experimental data. Finally, we give a brief summary and outlook in Sec. IV.

II. METHODS

Our first-principles calculations based on the density functional theory [20,21] have been performed using plane-wave basis, as implemented in the Vienna *ab initio* simulation package (VASP) [22,23]. We have used projector-augmented wave (PAW) [24,25] potentials in our calculations and the wave functions were expanded in the plane-wave basis with a kinetic energy cutoff of 500 eV. We used a generalized gradient approximation (GGA) with the Perdew-Burke-Ernzerhof (PBE) [26] parametrization for the exchange-correlation energy functional. Total energies were converged to less than 10^{-8} eV to achieve self-consistency and Brillouin zone integration was sampled on a Γ-centered k mesh of $6 \times 6 \times 6$. In structural relaxation, positions of the ions were relaxed toward the equilibrium using the conjugate gradient algorithm, until the Hellman-Feynman forces became less than 10^{-3} eV/Å.

Electron correlation effects beyond GGA were incorporated for $3d$ electrons of Mn and V ions within the GGA + U approximation. There are two approaches available for GGA + U calculations: (a) a spherically symmetric [27] scheme in which both U and J are independent, where U is the Hubbard parameter of on-site Coulomb correlation [28] and J is the Hund's coupling strength, and (b) a spherically averaged one with only one independent parameter $U_{\text{eff}} = U - J$ [29], which is clearly a special case and an approximation of the spherically symmetric scheme (a). As the spherically averaged scheme has been used in earlier studies with some success to capture experimental results for vibrational properties [30,31], we have used it here in our analysis. We note that results for phonons can be sensitive to the choice of values of the U and J parameters (see Sec. I of the Supplemental Material [32]), and the spherically symmetric approach with self-consistent choices of U and J is expected to give a more accurate description of phonons and electron spin-phonon couplings. We present below the results obtained within the spherically averaged GGA + U approach with $U = 5$ eV and $J = 1$ eV [29], assuming an A-type orbital order, which is consistent with the $I4_1/a$ space group symmetry of the low-temperature structure of MnV_2O_4 [17].

The dynamical matrix and phonons were calculated from a frozen-phonon method with atomic displacements of ±0.03 Å, as driven by the PHONOPY code [33], and Raman scattering intensity peaks were obtained from PHONON software [34] interfacing with DFT as implemented in the VASP code. The phonon density of states (DOS) has been calculated by using the tetrahedron method on a $10 \times 10 \times 10$ k mesh.

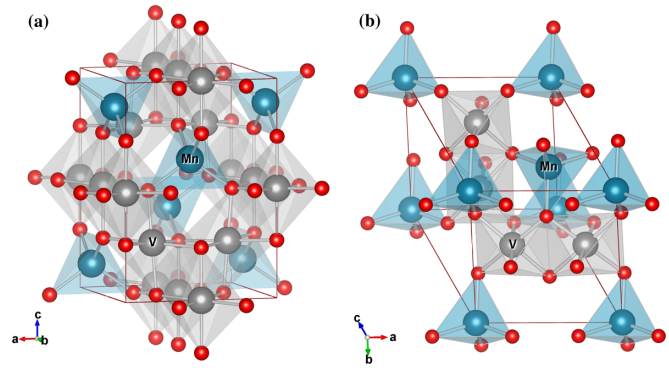

FIG. 1. (a) Crystallographic unit cell and (b) primitive cell of MnV_2O_4 compound. Oxygen octahedra (tetrahedra) around V (Mn) ions are shown in gray (cyan-blue).

Spin-phonon couplings were determined based on the scheme [35] used by Ray *et al.*

III. RESULTS AND DISCUSSION

A. Structural properties

The MnV_2O_4 compound, in its low-temperature phase, has a tetragonal structure with $I4_1/a$ space group symmetry. A network of edge-shared VO_6 octahedra with interstitial MnO_4 tetrahedra form a geometrically frustrated lattice in which the mirror or glide plane perpendicular to the ab plane is absent. The tetragonal unit cell of MnV_2O_4 is shown in Fig. 1(a). The lattice constants and the atomic positions are optimized within the GGA and GGA + U approximations to achieve the minimum energy structure. However, one can see imaginary frequencies in the phonon DOS [Fig. 2(a)] with the GGA-optimized structure, which may indicate that in GGA the assumed space group is unstable.

As the compound MnV_2O_4 is known to be a Mott insulator, strong correlation physics is incorporated in the calculations within the GGA + U approximation. The calculations have been performed for U_{eff} (= $U - J$, where U is the on-site Coulomb interaction and J is the Hund's exchange interaction) ranging from 3 eV to 5 eV at the Mn and V sites. For $U_{\text{eff}} \geqslant 4$ eV, we observe no imaginary modes in the DOS [Fig. 2(b)] and the results do not change significantly above that value. Therefore, we present the results obtained for $U_{\text{eff}} = 4$ eV at both sites. Atom projected phonon DOSs within GGA + U calculations for FiM and ferromagnetic (FM) spin states are shown in Fig. 2(c) and Fig. 2(d), respectively. To check the dependence of phonon properties on U values, we have also performed phonon calculations with different U values at Mn ($U = 6$ eV) and V ($U = 5$ eV) sites (see Sec. II of the Supplemental Material [32]). The phonon dispersion is similar to the dispersion obtained for $U_{\text{eff}} = 4$ eV and the physics discussed in the paper remains the same qualitatively.

In addition, we have considered collinear FiM ordering (V spins are aligned opposite to Mn spins) instead of the non-collinear magnetic ground state to reduce the computational cost. However, these two magnetic states are very close in energy as one can see from the transition temperatures [10], and the electronic properties (e.g., orbital ordering) [17,36]

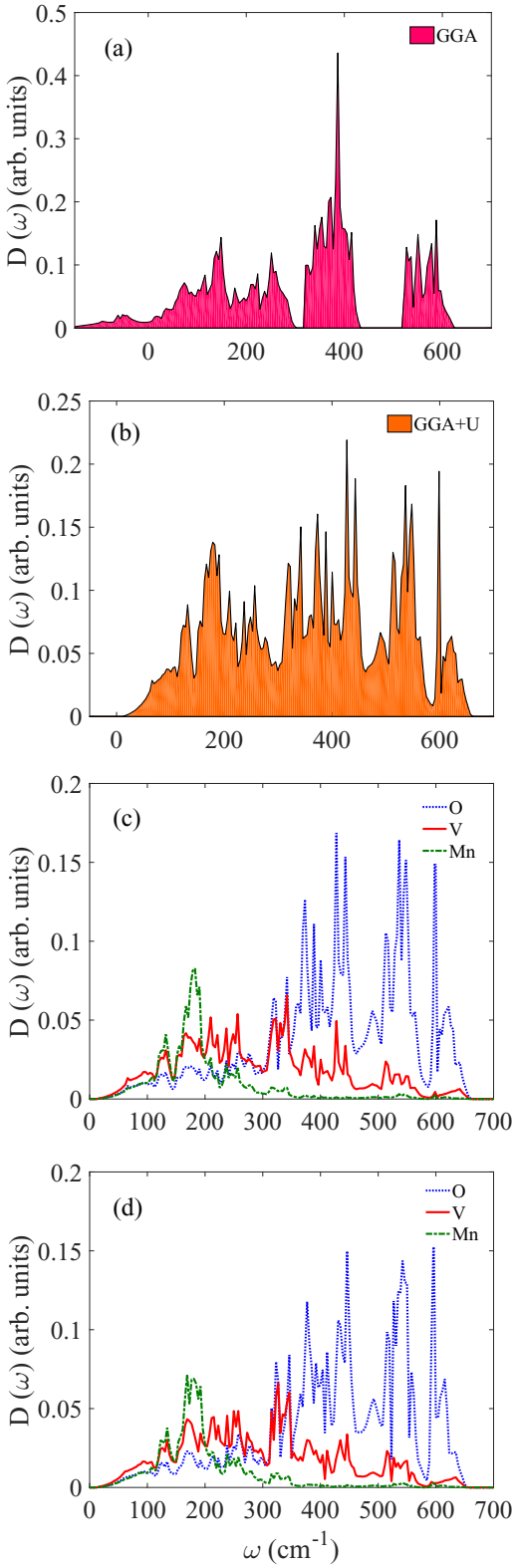

FIG. 2. Total phonon DOS is shown for (a) GGA and (b) GGA + U calculations in FiM configuration. Unstable modes with imaginary frequencies (given as negative) are observed only in GGA calculations. Projected DOS of Mn, V, and O atoms within GGA + U calculations in (c) FiM and (d) FM states.

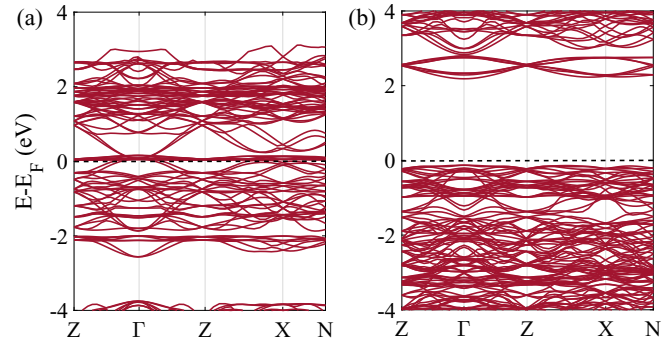

FIG. 3. Electronic band structure of MnV_2O_4 in FiM state within (a) GGA and (b) GGA + U calculations.

remain the same for both magnetic structures. Also, within the FiM spin configuration, the space group and the point group symmetry of the low-temperature crystal structure are preserved, reproducing the experimentally observed phonon modes.

It is evident from Fig. 3(a) that the electronic band structure of MnV_2O_4 shows zero band gap within GGA calculations. On the other hand, the GGA + U calculated electronic band structure [Fig. 3(b)] correctly represents the insulating state. We have also shown the atom projected electronic DOS [Figs. 4(a), 4(b)] for FiM and FM spin states within the GGA + U approximation. In both cases, the DOS shows the insulating state. Within the FiM spin configuration, we obtain the value of band gap ∼2 eV [Fig. 3(b)]. However, the calculated gap value is a bit high as compared to the activation energy (1.46 eV) of MnV_2O_4 [37].

In Table I, we compare the structural parameters of the GGA- and GGA + U-optimized structures for different spin configurations with the experimental one. We can see that the lattice constants, c/a ratio, and atomic positions of the optimized structures are comparable. The MnV_2O_4 compound in the tetragonal phase has C_{4h} point group symmetry and its primitive unit cell [see Fig. 1(b)] contains six magnetic ions (two Mn and four V) and eight nonmagnetic O ions. Phonons at the Γ point can be classified according to the irreducible representations of the C_{4h} point group of MnV_2O_4 as $\Gamma = 6E_u + 6A_u + 6B_u + 4B_g + 4E_g + 3A_g$, where the acoustic modes are omitted. Among them, the B_g, E_g, and A_g modes are Raman active, while the E_u and A_u modes are IR active.

B. Raman activity

In this section, we calculate the Raman spectra from density functional theory. The irreducible representation of Raman-active modes at the Γ point are listed in Table II along with the calculated phonon frequencies. Calculated Raman-allowed phonon modes are in good agreement with the experiments [18].

In a Raman scattering process, an incident photon of frequency ω_l and polarization versor $\mathbf{g}_l$ either create (Stokes process) or annihilate (anti-Stokes process) a phonon of frequency ω_j and scatter to an outgoing photon of frequency ω_s and polarization versor $\mathbf{g}_s$. From the principle of energy conservation, we can write $\omega_s = \omega_l \pm \omega_j$, where the (plus) minus

TABLE I. Energy-minimized structural parameters of MnV_2O_4 in the FiM and FM states within GGA and GGA+U approximations. Experimental structural parameters are given for comparison [11]. LCs = lattice constants.

	Experimental	GGA (FiM)	GGA+U (FiM)	GGA+U (FM)
LCs	$a = 6.05$ Å $c = 8.46$ Å	$a = 6.00$ Å $c = 8.48$ Å	$a = 6.19$ Å $c = 8.60$ Å	$a = 6.20$ Å $c = 8.61$ Å
Mn	0.000 0.750 0.875	0.000 0.750 0.875	0.000 0.750 0.875	0.000 0.750 0.875
V	0.250 0.250 0.750	0.250 0.250 0.750	0.250 0.250 0.750	0.250 0.250 0.750
O	0.997 0.474 0.737	0.999 0.478 0.739	0.993 0.474 0.739	0.993 0.474 0.739

sign is ascribed to the (anti-)Stokes process. The differential cross section for Raman scattering in nonresonant conditions of the Stokes process involving a phonon of eigenmode j is given by the following equation (for a unit volume of the sample) [38,39]:

$$\frac{d^2\sigma}{d\Omega d\omega} = \sum_j \frac{\omega_s^4}{c^4} |\mathbf{g}_s \cdot \bar{R}^j \cdot \mathbf{g}_l|^2 [n_b(\omega) + 1] \delta(\omega - \omega_j). \quad (1)$$

In this expression, $n_b(\omega)$ is the Bose occupation factor and c is the velocity of light in vacuum. The second-rank tensor $\bar{R}^j$ in Eq. (1) is known as the Raman tensor associated with the phonon eigenmode j which is given by the following equation:

$$R^j_{\alpha\beta} = \sqrt{\frac{V\hbar}{2\omega_j}} \sum_{\kappa=1}^{N} \frac{\partial \chi_{\alpha\beta}}{\partial \mathbf{r}(\kappa)} \cdot \frac{\mathbf{e}(j,\kappa)}{\sqrt{M_\kappa}} \quad (\alpha, \beta = 1, 2, 3). \quad (2)$$

Here, V is the unit cell volume. $\mathbf{r}(\kappa)$ and M_κ are the position and mass of the κ th atom, respectively, and the summation runs over all the N atoms in the unit cell. The eigenstates and eigenvalues of the dynamical matrix at the Γ point are denoted by $\mathbf{e}(j,\kappa)$ and ω_j, respectively. In Eq. (2), the electric polarizability tensor $\chi_{\alpha\beta}$ is defined as $\chi_{\alpha\beta} = \frac{1}{4\pi}(\epsilon_{\alpha\beta} - \delta_{\alpha\beta})$, where $\epsilon_{\alpha\beta}$ is the dielectric tensor. The tensor $\bar{R}^j$ is computed from the electric polarizability tensor within the finite-difference approach by moving the atoms of different symmetry with a displacement of 0.03 Å [40,41].

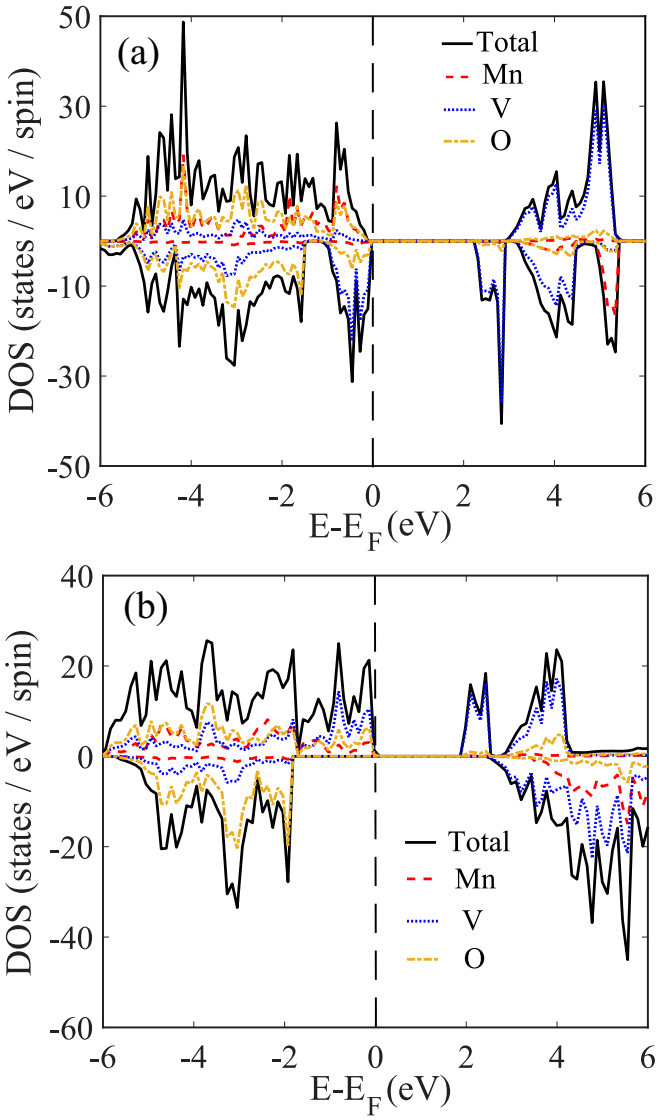

FIG. 4. Total and projected electronic DOS of Mn, V, and O atoms of MnV_2O_4 in (a) FiM and (b) FM states within GGA + U calculations. DOSs on the positive Y axis represent up-spin states, while DOSs on the negative Y axis represent down-spin states.

TABLE II. Irreducible representations of the Raman-active modes, calculated phonon frequencies (in cm^{-1}) for FiM and FM spin configurations in comparison with the Raman-active modes observed experimentally. The second column represents experimentally observed phonon frequencies [18]. Relative angular frequency shift ($\Delta_{rel} = \frac{\omega_{FiM} - \omega_{FM}}{\omega_{FiM}} \times 100\%$) due to change in magnetic ordering of the Raman-active modes is given in the fifth column.

Modes	Expt. ($T = 5$ K)	FiM (GGA+U)	FM (GGA+U)	Δ_{rel} (%)
$4B_g$		181	184	−1.7
	370	367	374	−1.9
	479	440	438	0.4
	585	539	538	0.2
$4E_g$		185	187	−1.1
		257	248	3.5
		451	449	0.4
	570	549	550	−0.2
$3A_g$		319	322	−0.9
		378	377	0.3
	673	633	623	1.6

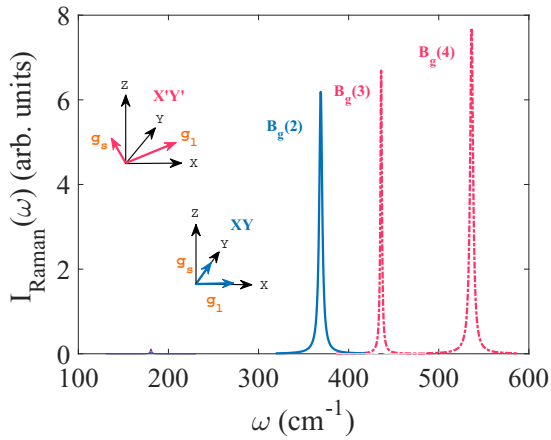

FIG. 5. Calculated Raman spectrum for light in the $X'Y'$ and XY polarization. Raman peaks with red (blue) color are observed in $X'Y'$ (XY) polarization.

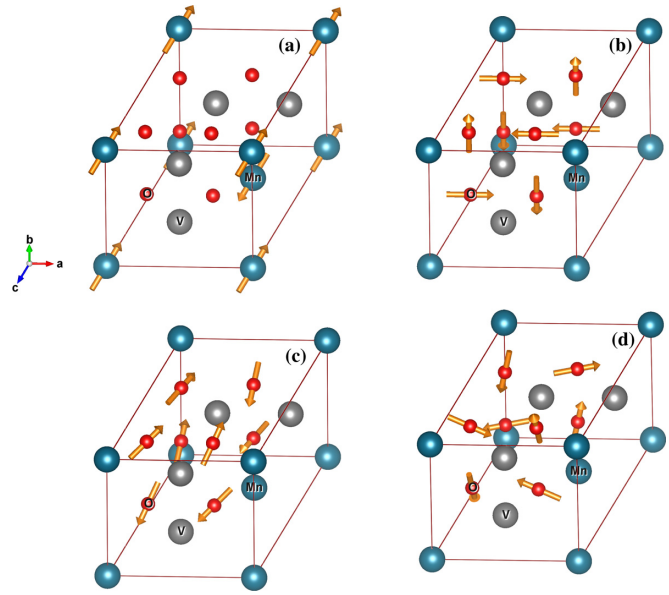

FIG. 6. Atomic displacements of B_g phonons responsible for the Raman peaks associated with the four B_g modes at (a) 181 cm^{-1} [$B_g(1)$], (b) 367 cm^{-1} [$B_g(2)$], (c) 440 cm^{-1} [$B_g(3)$], and (d) 539 cm^{-1} [$B_g(4)$].

In order to compare our theoretical results with the available experimental data, we have computed the intensity of the Raman spectra of a single-crystal sample from the differential scattering cross section as implemented in the PHONON software [34] at various polarization configurations of the incident and scattered light (same as the experimental ones [18]). In our calculations, we have considered linear polarization along the [100], [010], [110], and [1$\bar{1}$0] directions, which are ascribed to X, Y, X', and Y', respectively. The temperature dependence of the Raman spectra within the XY (polarization direction of the incident and scattered light, respectively) and $X'Y'$ polarization configurations has been reported experimentally, and by analyzing the intensity peaks of certain modes, the nature of the orbital ordering in this compound was established [18]. However, the phonon frequencies were calculated by assuming short-range force constants for the nearest-neighbor bonds and the modes were assigned (irreducible representation) based on the $I4_1/amd$ space group, while the space group symmetry of the parent compound is actually $I4_1/a$.

Calculated frequencies of the four Raman-allowed B_g modes within the $I4_1/a$ space group symmetry are at 181 cm^{-1} [$B_g(1)$], 367 cm^{-1} [$B_g(2)$], 440 cm^{-1} [$B_g(3)$], and 539 cm^{-1} [$B_g(4)$]. From our Raman scattering calculations, we found finite-intensity peaks in the $X'Y'$ polarization (Fig. 5) at two higher-frequency B_g modes [$B_g(3)$ and $B_g(4)$], while the lower modes [$B_g(1)$ and $B_g(2)$] are absent. This result agrees well with the experimental findings [18]. Interestingly, an intensity peak appears in XY polarization at 367 cm^{-1} (see Fig. 5) associated with the $B_g(2)$ mode. This mode is also observed experimentally at 370 cm^{-1} in the XY spectrum, while earlier theoretical calculations based on the Franck-Condon formalism predicted the absence of intensity peaks in the same polarization [18]. According to their theory, the Mott excitations along the in-plane V-V bond are allowed in the XY configuration and due to the symmetric nature of the d_{xy} orbital, Mott transitions to the forward and backward direction cancel the intensity [18].

We discuss the Raman peaks of the specific phonon modes of MnV_2O_4 in its tetragonal phase and understand the displacement patterns of the lattice vibrations obtained from *ab initio* phonon calculations. Among the four B_g modes, only three B_g modes show the finite intensity of the Raman peaks, while the first one [$B_g(1)$] does not contribute to the Raman scattering process. In Fig. 6, we have shown the displacement patterns of these modes. The $B_g(1)$ mode corresponds to the stretching of the Mn ions along the c direction [Fig. 6(a)]; the O ions barely move in this mode. We can see in Figs. 2(c) and 2(d) that phonons associated with the vibration of Mn ions contribute more to the DOS around that frequency range. The $B_g(2)$ [Fig. 6(b)] mode, responsible for the Raman peak at 367 cm^{-1}, comes from the displacements of the O ions along the a and b axes while the atomic vibrations of Mn ions are negligibly small. The modes $B_g(3)$ and $B_g(4)$, responsible for the Raman peaks at 440 cm^{-1} and 539 cm^{-1}, respectively, correspond to the displacements of O atoms as shown in Fig. 6(c) and Fig. 6(d). We have clearly shown here that the lowest frequency B_g mode emerges due to the phonons associated with Mn ions and high-frequency B_g modes originate from the atomic vibrations of O ions mainly. However, in all cases, V ions do not move.

C. Spin-phonon coupling

To understand the interplay between magnetic ordering and phonons, we determine phonons at the zone center and zone boundaries with FiM and FM ordering, which gives a measure of spin-phonon coupling. While any spin configuration instead of FM would have been also useful for this purpose, the space group symmetry remains the same in these spin configurations. In Fig. 7, we show phonon spectra along high-symmetry directions in the Brillouin zone for the FiM and FM spin-ordered states in the tetragonal phase of MnV_2O_4. In the absence of spin-phonon coupling, hardly any change in phonon spectra is expected in the different magnetic

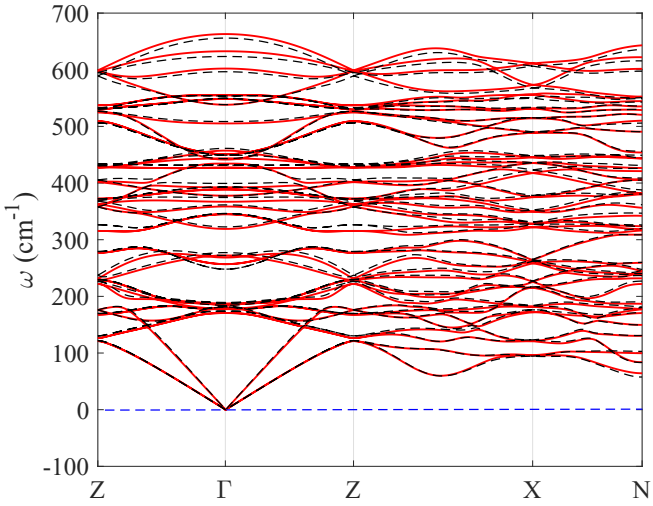

FIG. 7. Phonon dispersion of FiM (red solid lines) and FM (black dotted linens) states of MnV_2O_4 in its tetragonal phase.

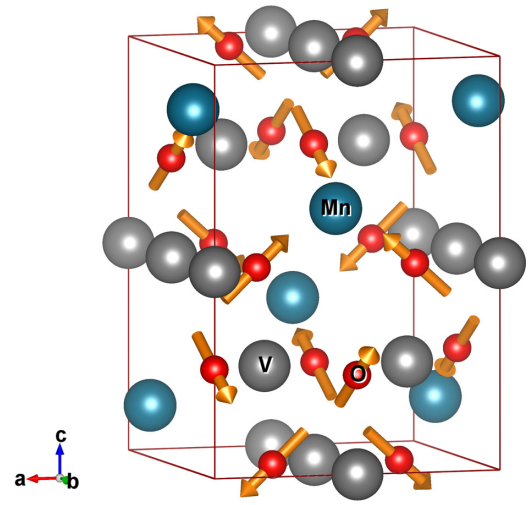

FIG. 8. The Hellman-Feynman forces on the oxygen ions in the FM configuration of the relaxed FiM configuration (crystallographic unit cell). The forces are drawn with golden arrows and give the lowest-order spin-phonon coupling.

configurations. A strong spin-phonon coupling along the zone center and zone boundary points is however observed as the phonon frequencies change with changing magnetic order. In the phonon dispersion (Fig. 7), no unstable modes appear at any point in the BZ for either magnetic order.

The Heisenberg spin Hamiltonian for MnV_2O_4 can be written as

$$H = \frac{1}{2}\sum_{\langle ij\rangle} J_{ij}\vec{S}_i \cdot \vec{\sigma}_j - \frac{1}{2}\sum_{\langle kl\rangle} J'_{kl}\vec{\sigma}_k \cdot \vec{\sigma}_l. \tag{3}$$

J_{ij} is the AFM exchange interaction between $\vec{S}_i$ (Mn spins) and $\vec{\sigma}_j$ (V spins) giving an FiM state, whereas J_{kl} is the FM exchange interaction between V spins. Changes in the exchange interactions due to the spin-phonon coupling can be obtained by a Taylor series expansion of J with respect to the amplitude of atomic displacements [42,43],

$$J(\vec{u}^{\lambda}_{\nu}) = J_0 + \vec{u}^{\lambda}_{\nu}\left(\nabla_{u_\nu} J\right) + \tfrac{1}{2}\vec{u}^{\lambda}_{\nu}(\nabla^2_{u_{\nu\nu'}} J)\vec{u}^{\lambda}_{\nu'}. \tag{4}$$

Here, $\vec{u}^{\lambda}_{\nu}$ is the displacement vector from the equilibrium position of the νth ion for the λth phonon mode. J_0 is the bare spin-spin exchange coupling term, and $\nabla_u J$ relates to the forces on atoms arising from the change in magnetic configuration (with respect to its ground state magnetic order). This term, which is linear in atomic displacements, gives the lowest-order coupling between spins and phonons. As seen in Fig. 8, these forces are equal and opposite for the pairs of oxygen atoms and also have the full symmetry (A_g) of the lattice. This could lead to the magnetoelastic anomaly at T_N. The shift in the phonon frequency Δ_λ of the λth phonon mode due to the change in the magnetic order is related to $\nabla^2_u J$ [42] (second-order coupling) by the following expression (the reduced mass and the frequency of the λth phonon mode are denoted by μ_λ and ω_λ, respectively, and $\hat{u}^{\lambda}_{\nu} = \vec{u}^{\lambda}_{\nu}/|\vec{u}^{\lambda}_{\nu}|$):

$$\Delta_\lambda = \frac{1}{2\mu_\lambda\omega_\lambda}\sum_{\nu}\hat{u}^{\lambda}_{\nu}\left(\nabla^2_{u_\nu} J\right)\hat{u}^{\lambda}_{\nu} = \frac{J''_\lambda}{2\mu_\lambda\omega_\lambda}. \tag{5}$$

This quantity gives an estimate of second-order spin-phonon coupling ($J''_\lambda = \sum_\nu \hat{u}^{\lambda}_{\nu}(\nabla^2_{u_\nu} J)\hat{u}^{\lambda}_{\nu}$ [44]), and hence, large values of Δ imply strong spin-phonon coupling. The relative change in phonon frequency ($\Delta^{\lambda}_{\rm rel} = \frac{\omega^{\lambda}_{\rm FiM} - \omega^{\lambda}_{\rm FM}}{\omega^{\lambda}_{\rm FiM}} \times 100\%$) [31] due to change in the magnetic order for the Γ ($\mathbf{q} = 0, 0, 0$) phonons, as well as for the zone boundary phonons at the N (1/2, 0, 0), X (0, 0, 1/2), and Z (1/2, 1/2, −1/2) points of the BZ, are presented in Figs. 9(a)–9(d).

In Fig. 9(a), two low-frequency (181 cm^{-1}, 367 cm^{-1}) B_g modes (all B_g modes are marked in red circles) show softening of frequency due to change in spin configuration from FM to FiM. However, two high-frequency B_g modes at 440 cm^{-1} and 549 cm^{-1} show very weak spin-phonon coupling compared to the others. Among all the Γ phonons, the B_u mode at 178 cm^{-1} (marked by sky-blue circles) shows maximum

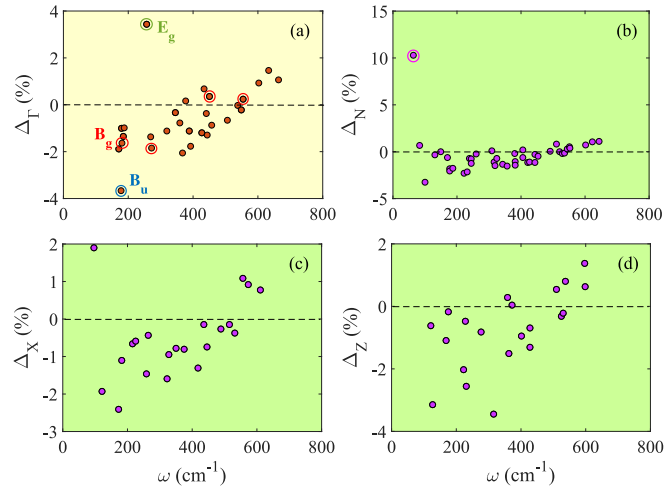

FIG. 9. Relative change in phonon frequency ($\Delta_{\rm rel} = \frac{\omega_{\rm FiM} - \omega_{\rm FM}}{\omega_{\rm FiM}} \times 100\%$) calculated at the zone center (a) Γ and zone boundary points (b) N, (c) X, (d) Z.

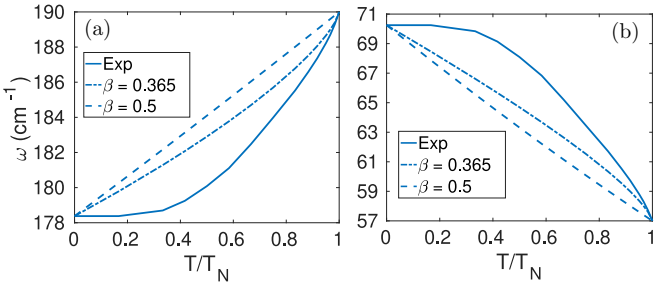

FIG. 10. Temperature dependence of phonon modes [(a) 178 cm^{-1} (for $\Delta_\lambda = -6$ cm^{-1}) and (b) 70 cm^{-1} (for $\Delta_\lambda = 7$ cm^{-1})] obtained for three choices of $m(T)$ (see text). "Exp" refers to use of experimental $m(T)$ [45] in our analysis [Eq. (7)] to determine $\omega(T)$ corresponding to FiM spin ordering, and β is the critical exponent.

relative softening ($\sim -4\%$), while the 257 cm^{-1} E_g mode (marked by green circles) shows maximum relative hardening due to spin-phonon interaction. Among the zone boundary phonons, the 70 cm^{-1} phonon mode (pink circles) [Fig. 9(b)] at the N point of the BZ $(1/2, 0, 0)$ shows more than 10% hardening of frequency due to change in magnetic order from FM to FiM and exhibits the strongest spin-phonon coupling across the BZ.

To connect our results with experiments [19] and to understand the observed temperature dependence of phonon frequencies, we use Ginzburg-Landau (GL) theory. The free energy of our spin-phonon coupled system can be written as

$$F = F_0 + am^2 + bm^4 + \sum_\lambda \left(J''_\lambda m^2 v_\lambda^2 + \frac{1}{2}\mu_\lambda \omega_{0\lambda}^2 v_\lambda^2 \right). \quad (6)$$

Here, a and b are the usual GL parameters, m is the FiM order parameter, v_λ is the amplitude of the λth phonon mode, and $\omega_{0\lambda}$ is the high-temperature ($T \geqslant T_N$) phonon frequency. Thus, the phonon frequency will change below T_N as the FiM ordering sets in. The modified phonon frequency is

$$\omega_\lambda = \sqrt{\omega_{0\lambda}^2 + \frac{2}{\mu_\lambda} J''_\lambda m^2} = 2\Delta_\lambda m^2 + \sqrt{\omega_{0\lambda}^2 + 4\Delta_\lambda^2 m^4}. \quad (7)$$

Here, the positive solution has been considered, as the other solution gives negative values of ω_λ. We determine the Δ_λ's from results of our DFT calculations (Fig. 9) and use them in Eq. (7) to obtain the temperature dependence of relevant phonon frequencies (Fig. 10) of the tetragonal phase of MnV_2O_4 using three choices of temperature-dependent FiM order parameter $m(T)$: one taken from experiment [45] and the other two are based on an approximate model form given by $\propto (1 - T/T_N)^\beta$, with the critical exponent $\beta = 0.5$ (the mean-field behavior) and $\beta = 0.365$ (3D Heisenberg model [46] behavior). The experimental $m(T)$ used in this analysis was recorded at magnetic field $H = 3$ T, which stabilizes the FiM state of MnV_2O_4 at lower temperatures. It is quite clear (Fig. 10) that the temperature dependence of phonon frequencies arising from spin-phonon coupling obtained with experimental $m(T)$ agrees rather well with experimental $\omega(T)$ (in Figs. 1(e), 1(f) and 1(g) of Ref. [19]). This shows that the spin-phonon coupling is primarily responsible for T dependence of the relevant phonons in MnV_2O_4 at low temperature.

In Fig. 10(a), the phonon frequency decreases with decreasing temperature below T_N, which is associated with the softening of a phonon mode ($\Delta_\lambda < 0$) due to spin-phonon coupling. Interestingly, in the Raman scattering experiments [18,19], the intensity peak near 178 cm^{-1} shows anomalous temperature dependence as the frequency decreases with decreasing temperature below T_N. In Fig. 10(b), one can see that the phonon frequency increases with decreasing temperature below T_N and this is associated with the hardening of a phonon mode ($\Delta_\lambda > 0$) due to coupling between spins and phonons. Experimentally, the temperature dependence of the Raman intensity peak near 70 cm^{-1} shows a similar behavior below the FiM transition temperature. However, these two peaks are attributed to the magnon excitations, with Raman-allowed symmetries [19]. They couple to phonons exhibiting strong spin-phonon coupling. Even though 70 cm^{-1} and 178 cm^{-1} modes are not Raman active, they show significant spin-phonon coupling. Thus, magnetic excitations couple with these modes, and the hybrid modes appear in the Raman spectrum. Our results agree qualitatively with the experimental observations and also corroborate the experimental prediction of strong spin-lattice coupling across the BZ in this material.

IV. CONCLUSIONS

Our first-principles study of phonon dispersions in two different magnetic orders (FiM and FM) in MnV_2O_4 show notable spin-phonon coupling. We also find that in the low-temperature tetragonal structure of MnV_2O_4, correlations are necessary to eliminate unstable modes. Raman intensities for XY and $X'Y'$ polarization reveal finite-intensity peaks in the $X'Y'$ polarization at two higher-frequency B_g modes [$B_g(3)$ and $B_g(4)$] and a peak in XY polarization at 367 cm^{-1}, which is associated with the $B_g(2)$ mode. The lowest-frequency B_g mode is found to emerge from phonons associated with Mn ions, while high-frequency B_g modes originate from O ion vibration. Landau theory analysis reveals the mechanism governing the low-temperature Raman anomalies of MnV_2O_4. Our results agree qualitatively with recent experiments [18,19] and reveal that a strong interplay between the lattice and magnetic degrees of freedom is important for understanding the underlying physics of MnV_2O_4.

ACKNOWLEDGMENTS

D.D. acknowledges the Department of Science and Technology (DST), India, for support from an INSPIRE research fellowship. U.V.W. acknowledges support from a J. C. Bose National Fellowship and a Sheikh Saqr Fellowship. A.T. acknowledges research funding from CSIR (India) through Grant No. 03(1373)/16/EMR-II.

[1] Y. Tokura and N. Nagaosa, Science **288**, 462 (2000).

[2] S.-H. Lee, H. Takagi, D. Louca, M. Matsuda, S. Ji, H. Ueda, Y. Ueda, T. Katsufuji, J.-H. Chung, S. Park,

S.-W. Cheong, and C. Broholm, J. Phys. Soc. Jpn. **79**, 011004 (2010).
[3] P. G. Radaelli, New J. Phys. **7**, 53 (2005).
[4] D. I. Khomskii and T. Mizokawa, Phys. Rev. Lett. **94**, 156402 (2005).
[5] Y. Kato, G.-W. Chern, K. A. Al-Hassanieh, N. B. Perkins, and C. D. Batista, Phys. Rev. Lett. **108**, 247215 (2012).
[6] H. Tsunetsugu and Y. Motome, Phys. Rev. B **68**, 060405(R) (2003).
[7] D. Choudhury, T. Suzuki, D. Okuyama, D. Morikawa, K. Kato, M. Takata, K. Kobayashi, R. Kumai, H. Nakao, Y. Murakami, M. Bremholm, B. B. Iversen, T. Arima, Y. Tokura, and Y. Taguchi, Phys. Rev. B **89**, 104427 (2014).
[8] S.-H. Lee, D. Louca, H. Ueda, S. Park, T. J. Sato, M. Isobe, Y. Ueda, S. Rosenkranz, P. Zschack, J. Íñiguez, Y. Qiu, and R. Osborn, Phys. Rev. Lett. **93**, 156407 (2004).
[9] G. J. MacDougall, V. O. Garlea, A. A. Aczel, H. D. Zhou, and S. E. Nagler, Phys. Rev. B **86**, 060414(R) (2012).
[10] V. O. Garlea, R. Jin, D. Mandrus, B. Roessli, Q. Huang, M. Miller, A. J. Schultz, and S. E. Nagler, Phys. Rev. Lett. **100**, 066404 (2008).
[11] Y. Nii, H. Sagayama, T. Arima, S. Aoyagi, R. Sakai, S. Maki, E. Nishibori, H. Sawa, K. Sugimoto, H. Ohsumi, and M. Takata, Phys. Rev. B **86**, 125142 (2012).
[12] O. Tchernyshyov, Phys. Rev. Lett. **93**, 157206 (2004).
[13] S. Di Matteo, G. Jackeli, and N. B. Perkins, Phys. Rev. B **72**, 020408(R) (2005).
[14] T. Suzuki, M. Katsumura, K. Taniguchi, T. Arima, and T. Katsufuji, Phys. Rev. Lett. **98**, 127203 (2007).
[15] K. Adachi, T. Suzuki, K. Kato, K. Osaka, M. Takata, and T. Katsufuji, Phys. Rev. Lett. **95**, 197202 (2005).
[16] S. Sarkar, T. Maitra, R. Valentí, and T. Saha-Dasgupta, Phys. Rev. Lett. **102**, 216405 (2009).
[17] D. Dey, T. Maitra, and A. Taraphder, Phys. Rev. B **93**, 195133 (2016).
[18] K. Takubo, R. Kubota, T. Suzuki, T. Kanzaki, S. Miyahara, N. Furukawa, and T. Katsufuji, Phys. Rev. B **84**, 094406 (2011).
[19] S. L. Gleason, T. Byrum, Y. Gim, A. Thaler, P. Abbamonte, G. J. MacDougall, L. W. Martin, H. D. Zhou, and S. L. Cooper, Phys. Rev. B **89**, 134402 (2014).
[20] W. Kohn and L. J. Sham, Phys. Rev. **140**, A1133 (1965).
[21] P. Hohenberg and W. Kohn, Phys. Rev. **136**, B864 (1964).
[22] G. Kresse and J. Furthmüller, Phys. Rev. B **54**, 11169 (1996).
[23] G. Kresse and J. Furthmüller, Comput. Mater. Sci. **6**, 15 (1996).
[24] P. E. Blöchl, Phys. Rev. B **50**, 17953 (1994).
[25] G. Kresse and D. Joubert, Phys. Rev. B **59**, 1758 (1999).
[26] J. P. Perdew, K. Burke, and M. Ernzerhof, Phys. Rev. Lett. **77**, 3865 (1996).
[27] A. I. Liechtenstein, V. I. Anisimov, and J. Zaanen, Phys. Rev. B **52**, R5467 (1995).
[28] J. Hubbard, Proc. R. Soc. London A **276**, 238 (1963).
[29] S. L. Dudarev, G. A. Botton, S. Y. Savrasov, C. J. Humphreys, and A. P. Sutton, Phys. Rev. B **57**, 1505 (1998).
[30] U. D. Wdowik and K. Parlinski, Phys. Rev. B **75**, 104306 (2007).
[31] B. Paul, S. Chatterjee, A. Roy, A. Midya, P. Mandal, V. Grover, and A. K. Tyagi, Phys. Rev. B **95**, 054103 (2017).
[32] See Supplemental Material at http://link.aps.org/supplemental/10.1103/PhysRevB.101.205132 for more results from different calculations.
[33] A. Togo and I. Tanaka, Scr. Mater. **108**, 1 (2015).
[34] K. Parlinski, PHONON Software, Kraków, 2013.
[35] N. Ray and U. V. Waghmare, Phys. Rev. B **77**, 134112 (2008).
[36] J. Krishna, N. Singh, S. Shallcross, J. K. Dewhurst, E. K. U. Gross, T. Maitra, and S. Sharma, Phys. Rev. B **100**, 081102(R) (2019).
[37] V. Pardo, S. Blanco-Canosa, F. Rivadulla, D. I. Khomskii, D. Baldomir, H. Wu, and J. Rivas, Phys. Rev. Lett. **101**, 256403 (2008).
[38] M. Cardona and G. Güntherodt, *Light Scattering in Solids II* (Springer, Berlin, 1982).
[39] P. Brüesch, *Phonons: Theory and Experiments II* (Springer, Berlin, 1986).
[40] P. Umari, A. Pasquarello, and A. Dal Corso, Phys. Rev. B **63**, 094305 (2001).
[41] M. Ceriotti, F. Pietrucci, and M. Bernasconi, Phys. Rev. B **73**, 104304 (2006).
[42] E. Granado, A. García, J. A. Sanjurjo, C. Rettori, I. Torriani, F. Prado, R. D. Sánchez, A. Caneiro, and S. B. Oseroff, Phys. Rev. B **60**, 11879 (1999).
[43] P. Kumar, A. Bera, D. V. S. Muthu, S. N. Shirodkar, R. Saha, A. Shireen, A. Sundaresan, U. V. Waghmare, A. K. Sood, and C. N. R. Rao, Phys. Rev. B **85**, 134449 (2012).
[44] A. Kumar, C. J. Fennie, and K. M. Rabe, Phys. Rev. B **86**, 184429 (2012).
[45] K. Myung-Whun, J. S. Kim, T. Katsufuji, and R. K. Kremer, Phys. Rev. B **83**, 024403 (2011).
[46] L. Zhang, J. Fan, L. Li, R. Li, L. Ling, Z. Qu, W. Tong, S. Tan, and Y. Zhang, Europhys. Lett. **91**, 57001 (2010).